Chemical Science

ROYAL SOCIETY OF CHEMISTRY

EDGE ARTICLE

View Article Online
View Journal | View Issue

Open Access Article. Published on 05 May 2025. Downloaded on 4/1/2026 6:31:56 PM.
This article is licensed under a Creative Commons Attribution-NonCommercial 3.0 Unported Licence.

Check for updates

Cite this: *Chem. Sci.*, 2025, **16**, 11027

All publication charges for this article have been paid for by the Royal Society of Chemistry

A competition between 2D and 3D magnetic orderings in novel mixed valent copper frameworks†

Yao Abusa,[a] Joshua Greenfield,[c] Gayatri Viswanathan,[ab] Smitakshi Goswami,[d] Emma Ross,[a] Philip Yox,[ab] Richeal Oppong,[ae] Iyanu Ojo,[a] Jifeng Liu,[f] Andrew Ozarowski[g] and Kirill Kovnir*[ab]

Low-dimensional hybrid inorganic–organic frameworks exhibit high structural flexibility and allow for the inclusion of various magnetic and optically-active species into their host structures. The emergence of copper-based hybrid structures for various optical applications provides a promising foundation for exploring the integration of magnetic sublattices, paving the way for advancements in magneto-optical coupling and multifunctional materials. Herein, we introduce a novel class of hybrid copper frameworks with covalently-connected alternating magnetic 2D copper(II) formate and non-magnetic copper(I) bromide layers. The anionic framework is stabilized by A^+ cations to form $ACu_5Br_4(COOH)_4$ ($A^+ = Na^+$, K^+, Rb^+, NH_4^+) semiconductors (bandgaps 2.1–2.2 eV) with optical transitions suitable for optoelectronic applications. Comprehensive magnetometry studies show that $ACu_5Br_4(COOH)_4$ compounds exhibit low-dimensional 2D short-range antiferromagnetic order within the formate layers, characterized by strong exchange coupling ($J/k_B \sim -100$ K). Upon further temperature reduction, interactions between Cu(II) layers give rise to 3D long-range magnetic order at ~40 K, despite the large (8.6–8.8 Å) spatial separation of the magnetic Cu(II) formate layers by nonmagnetic Cu(I)–Br bridging layers. This transition is further supported by electron paramagnetic resonance (EPR) spectroscopy. This study expands our understanding of low-dimensional hybrid frameworks and opens new avenues for the design of 2D multifunctional materials.

Received 21st January 2025
Accepted 2nd May 2025

DOI: 10.1039/d5sc00548e

rsc.li/chemical-science

1 Introduction

The study of low-dimensional inorganic magnetic materials has been an exciting area of research for physicists and chemists. These materials exhibit a wide range of phenomena driven by their electronic configuration and arrangement of magnetic ions.[1,2] While inorganic magnets hold great potential for various applications, most reported phases consist of all-inorganic components with limited chemical tunability and processability.[3–6] Additionally, their inherently dense structures result in high material weight, restricting their suitability for applications that require lightweight and portable designs, such as wearable electronics or compact energy-efficient devices.[4] As a solution, researchers have been focusing on exploring hybrid inorganic–organic frameworks that can produce single molecules, 1D chains, 2D layered materials, and 3D networks with unique magnetic and optical properties.[2,7–14] These hybrid metal–organic materials have exhibited fascinating multifunctional properties, including long-range magnetic order, ferroelectricity, photo-absorption, and electronic conductivity, which are valuable in spintronics, multiferroics, and optical and quantum applications and devices.[15–22] Recently, there has been a lot of interest in the magnetic properties of materials with a layered copper(II) sublattice, mainly due to its relationship with quantum fluctuation and magnetic anisotropy.[23–25] The unique spin quantum number ($S = \frac{1}{2}$) and Jahn–Teller distortion of Cu(II) ions leads to intriguing behaviors that have potential implications for developing new materials.[26–29] Moreover, these materials can yield geometrically frustrated systems, giving rise to exciting quantum phenomena at low temperatures.[28,30] Copper-based

[a]Department of Chemistry, Iowa State University, Ames, Iowa 50011, USA. E-mail: kovnir@iastate.edu
[b]Ames National Laboratory, U.S. Department of Energy, Ames, Iowa 50011, USA
[c]Department of Chemistry, University of California, Davis, California 95616, USA
[d]Department of Physics and Astronomy, Dartmouth College, Hanover, NH 03755, USA
[e]Department of Materials Science and Engineering, Iowa State University, Ames, Iowa 50011, USA
[f]Thayer School of Engineering, Dartmouth College, Hanover, NH 03755, USA
[g]National High Magnetic Field Laboratory, Florida State University, Tallahassee, Florida 32310, USA

† Electronic supplementary information (ESI) available: Description of synthetic and characterization experimental procedures and additional figures and tables pertaining to powder X-ray diffraction, Rietveld refinement of synchrotron powder diffraction patterns, thermogravimetric (TG-DSC) analysis, BVS calculations, crystallographic files and data information for $ACu_5Br_4(COOH)_4$ ($A^+ = Na^+$, K^+, NH_4^+, Rb^+), SEM/EDS, and CHNO elemental analysis, and magnetic and EPR studies. CCDC 2412816–2412819. For ESI and crystallographic data in CIF or other electronic format see DOI: https://doi.org/10.1039/d5sc00548e

© 2025 The Author(s). Published by the Royal Society of Chemistry

Open Access Article. Published on 05 May 2025. Downloaded on 4/1/2026 6:31:56 PM. This article is licensed under a Creative Commons Attribution-NonCommercial 3.0 Unported Licence.

metal–organic materials offer an opportunity to implement strong magnetic coupling originating from magnetic exchange interactions between Cu^{2+} spin centers and organic linkers.

The length of linkers used in constructing magnetic coordination polymers affects the strength of magnetic coupling. Short ligands such as cyanide, azide, and formate are effective in promoting strong magnetic exchange coupling between metal centers, unlike their long-chain counterparts which can reduce coupling between moment carriers in the materials.[23,29,31–34] As the smallest carboxylate, the formate ion acts as either a single-atom connector (similar to the azide and cyanide) or a three-atom linker – making it an excellent choice for facilitating strong exchange coupling between metal centers.[7,8,33,35–40] The multiple bridging modes of the formate ion can facilitate ferro- (FM) or antiferromagnetic (AFM) coupling between metal centers, depending on the type of bridging and the identity of the metal atoms.[29,35] The coupling is due to the delocalization of electrons in the formate anion, which enables the transfer of π-electrons to neighboring metal ions when excited.[29] Apart from Ca- and Sr- copper formate salts, there are limited options for first-row transition metal formates without co-ligands.[7,8,41–44] The well-known families of homoleptic Cu-formates includes ferromagnetic 3D framework α-$Cu(COOH)_2$ and chain-like β-$Cu(COOH)_2$.[45] Some homoleptic Mn, Ni, Mg, Fe, and Co-formates, with the general formula $M_3(COOH)_6$ have recently been reported with varying magnetic properties.[10,46] While long-range antiferromagnetic ordering has been observed in some of these Fe, Co, and Ni-based formates their magnetic ordering is confined to the intralayer metal ions with weak magnetic features due to weak interlayer interactions in these compounds.[47,48] As a result, the search for materials with both intra (2D) and interlayer (3D) exchange interactions, resulting in intriguing magnetic properties, is in high demand.

Herein, we report a novel series of copper formate compounds that interconnect 2D copper(II) formate and copper(I) bromide layers to generate a 3D anionic framework. The anionic framework is stabilized by the intercalation of A^+ cations ($A^+ = Na^+, K^+, Rb^+, NH_4^+$) between Cu-formate/Cu–Br/Cu-formate trilayers. We detail the synthesis and structural characterization of $ACu_5Br_4(COOH)_4$ using various techniques including single-crystal and synchrotron powder X-ray diffraction, thermogravimetric analysis, infrared spectroscopy, and scanning electron microscopy. We also explore the optical and magnetic properties of the synthesized compounds *via* magnetometry, electron paramagnetic resonance spectroscopy (EPR), and linear optical property measurements. The outcomes of this study provide insight into the relationship between the structure and properties of these exciting copper formate/bromide materials and how the connectivity between alternating copper formate layers affects the magnetic and optical properties of the resulting compounds.

2 Experimental section

2.1 Safety warning

Solvothermal vessels may develop high autogenic pressures, which can result in the release of hot pressurized hazardous formic acid vapors during the reaction. Splashing of the ethanol/formic acid may occur upon opening of the reaction vessels, causing severe burns. It is highly recommended to wear proper personal protective equipment, such as face shields, long-sleeve gloves, and tight-cuff lab coats; to place the reaction vessels in secondary containment and allow them to cool to room temperature before opening; and to keep furnaces in well-ventilated spaces such as fume hoods.

2.2 Starting materials

Copper(II) bromide (Alfa Aesar, 99%), ammonium carbonate (Sigma-Aldrich, ≥30% NH_3 basis), sodium carbonate (Alfa Aesar, 99+%), potassium carbonate (Sigma-Aldrich, 99%), rubidium carbonate (Alfa Aesar, 99%), formic acid (Acros Organics, 99%), and 200-proof ethanol were used as received without further purification.

2.3 Synthesis of $ACu_5Br_4(COOH)_4$ ($A^+ = Na^+, K^+, Rb^+, NH_4^+$)

To synthesize $ACu_5Br_4(COOH)_4$, a solvothermal method was utilized. 25 mL pyrex media bottles (Fig. S1†) were loaded with 2 mmol of $CuBr_2$ and 0.5 mmol of alkali metal/ammonium carbonate (A_2CO_3). The vessels were then taken into a well-ventilated fume hood, where 5 mL of formic acid (HCOOH) and 5 mL of ethanol (C_2H_5OH) were added to the vessels. Right after, the vessels were tightly sealed with a GL25 PTFE-lined silicone septum cap to prevent over-pressurization during the reaction (Fig. S1†). An instant release of CO_2 gas occurs due to the reaction between carbonates and formic acid. Therefore, it is essential to perform the solvent process in a well-ventilated fume hood to avoid direct exposure to CO_2 gas. The reactant vessels were then placed in a solvothermal furnace, rapidly heated up to 70 °C, and then slowly cooled to 50 °C at a rate of 1 °C h^{-1}, and further cooled to room temperature by turning off the furnace. The resulting products were filtered and washed with 200-proof ethanol to obtain dark yellow plates of varying sizes (ranging from 0.5 × 0.5 mm^2 to 3 × 3 mm^2). The syntheses of lithium (Li) and cesium (Cs) analogs using the appropriate carbonate precursors were unsuccessful. All processes were performed under ambient conditions.

2.4 Characterization

The characterizations of solid samples, both single crystals and polycrystalline powders, were conducted using in-house and high-resolution synchrotron powder X-ray diffraction (PXRD), single-crystal X-ray diffraction (SCXRD), scanning electron microscopy coupled with energy dispersive X-ray spectroscopy (SEM/EDS), solid-state diffuse reflectance spectroscopy, Fourier transform infrared (FTIR) spectroscopy, as well as thermogravimetric analysis, and differential scanning calorimetry (TGA-DSC). SQUID magnetometry and electron paramagnetic resonance (EPR) spectroscopy were employed to investigate the magnetic properties of samples, while photoluminescence (PL) measurements elucidated optical behavior. Detailed descriptions of the experimental methodologies are available in the ESI.†

 © 2025 The Author(s). Published by the Royal Society of Chemistry

Open Access Article. Published on 05 May 2025. Downloaded on 4/1/2026 6:31:56 PM.
This article is licensed under a Creative Commons Attribution-NonCommercial 3.0 Unported Licence.

3 Results and discussion

3.1 Synthesis

Hybrid metal–organic frameworks are attractive for their intriguing physical properties, as well as their accessibility *via* low-temperature synthesis using earth-abundant reactants. By treating $CuBr_2$ in formic acid and ethanol with the addition of monovalent A^+ carbonate salt ($A^+ = Na^+, K^+, NH_4^+, Rb^+$) and slowly cooling the reaction mixture from 70 °C to 50 °C, large crystals of $ACu_5Br_4(COOH)_4$ were produced. Selected crystals were ground for in-house and synchrotron-based powder diffraction studies to confirm phase purity (Fig. 1a and S3†). The morphology and elemental composition of the products were studied using a SEM equipped with an EDS detector (Fig. 1b). Because EDS cannot reliably quantify low atomic weight elements such as C, O, N, and H, CHN/O organic component analysis was conducted to confirm the light element content (Table S1†).

The size of the crystallites can be controlled by adjusting the cooling rate of the reaction. For instance, reactions at a cooling rate of 2 °C h^{-1} produced smaller crystallites, while a cooling rate of 0.5 °C h^{-1} formed larger crystallites. The resulting compounds contained Cu^{2+} and Cu^{1+} cations, as determined from single-crystal diffraction analysis (discussed later), indicating a partial reduction of $CuBr_2$, likely facilitated by formic acid and/or alcohol. However, the exact reduction mechanism remains unknown. Reactions in the absence of alcohol (ethanol) do not result in the formation of the target phase, instead producing light blue crystallites of copper formate. The use of water as a substitute for alcohol yielded a dark-brown solution without any observable solid precipitate. The presence of absorbed moisture from the reaction atmosphere and the addition of a sacrificial amount of water (~100 μL) did not impact the integrity of target compounds or the size of crystallites (Fig. S2a†), in sharp contrast with previously reported syntheses of formate-based compounds.[49,50] Switching from ethanol to 1-butanol did not significantly impact the formation of the target compound (Fig. S2b†). Therefore, the target hybrid compounds can be synthesized under ambient conditions as the presence of absorbed moisture, water of hydration from metal salts, and the addition of sacrificial water do not impede formation of the target phase, nor does the type of primary alcohol used.

3.2 Crystal structure description

Crystal structures of $ACu_5Br_4(COOH)_4$ compounds were solved from single crystal X-ray diffraction (SCXRD) data. The validity of the resulting structural models was confirmed by refining high-resolution powder X-ray diffraction data (PXRD) (Fig. 1a and S3†). All bond distances discussed herein correspond to those observed in the refined single crystal data. All $ACu_5Br_4(COOH)_4$, except $A^+ = Na^+$, crystallize in the monoclinic centrosymmetric space group $C2/m$ (Fig. 2). In the layered crystal structure, copper(II) formate layers are linked to Cu(I) bromide layers *via* Cu(II)–Br–Cu(I) covalent bridges (Fig. 2c). Cu(II)formate–Cu(I)Br–Cu(II)formate slabs are separated by layers of monovalent A^+ cations. The asymmetric unit has four distinct Cu sites: three Cu^+ and one Cu^{2+} site. The oxidation state assignments of Cu^+ and Cu^{2+} were determined based on bond valence sum (BVS) calculations derived from refined single-crystal data (Table S6†). The Cu^+ atoms occupy the Wyckoff sites 4*h*, 4*h*, and 8*j*, with 75% occupancy each, resulting in three Cu^+ ions per formula unit ($Z = 4$). These Cu^+ ions are coordinated by four bromine atoms in a distorted tetrahedral environment (Fig. 2a) with Cu–Br distances ranging from 2.47 to 2.51 Å and Br–Cu–Br angles ranging from 104.38(1) to 115.47(1)°. Cu2/Cu4 (4*h* sites) double tetrahedra share edges to form 1D chains propagating along the [010] direction. These chains further share edges with chains of Cu3 (8*j* site) tetrahedra, resulting in infinite 2D $[(0.75Cu)_4Br_4]^{1-}$ layers propagating within the *ab*-plane (Fig. 2e).

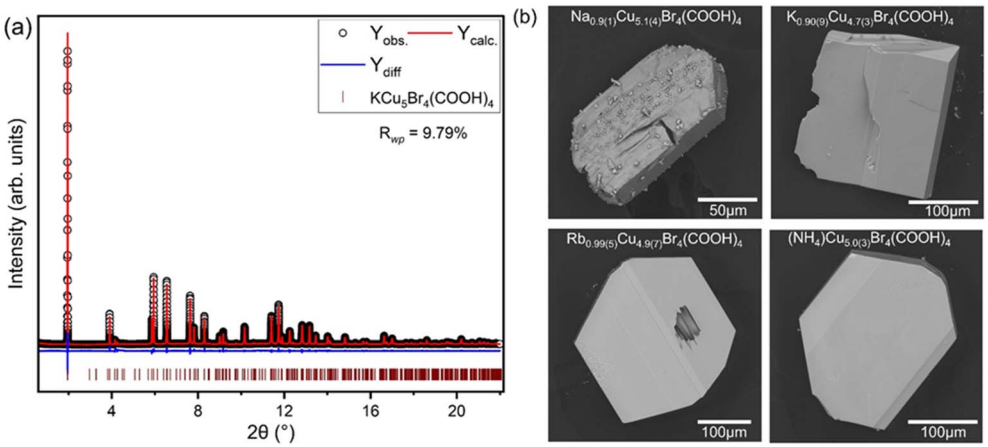

Fig. 1 (a) Rietveld refinement of room-temperature synchrotron PXRD data ($\lambda = 0.412642$ Å) for $KCu_5Br_4(COOH)_4$. Experimental data: black open circles. Calculated pattern: red line. Difference profile: blue. Vertical maroon ticks indicate the positions for $KCu_5Br_4(COOH)_4$ reflections (space group: $C2/m$, no. 12). (b) SEM backscattered electron images of selected crystals of $ACu_5Br_4(COOH)_4$ with respective compositions. The heavy elements (Cu, Rb/K/Na, Br) were determined from EDS and normalized to 4 Br atoms, while lighter elements (C, H, N, O) are determined from CHN/O analysis and normalized to the total molecular weight of the respective compounds.

Open Access Article. Published on 05 May 2025. Downloaded on 4/1/2026 6:31:56 PM.
This article is licensed under a Creative Commons Attribution-NonCommercial 3.0 Unported Licence.

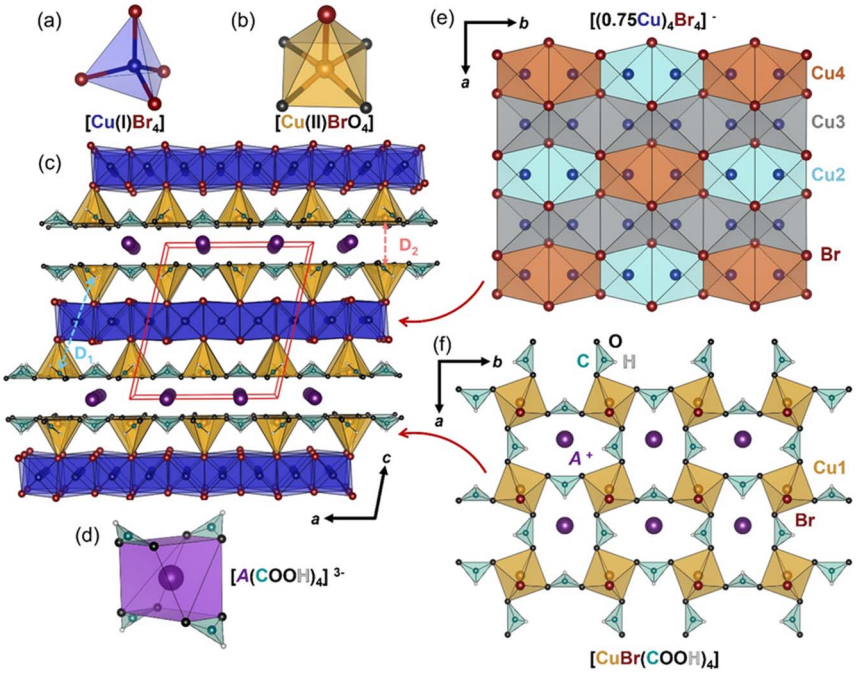

Fig. 2 The structure of $ACu_5Br_4(COOH)_4$ featuring (a) [Cu(I)Br_4] tetrahedra and (b) square pyramidal [Cu(II)BrO_4] building units. (c) General view of the layered structure emphasizing the connectivity between the Cu-based layers. The unit cell is outlined in red. Two different Cu(II)–Cu(II) interlayer distances are labelled as D_1 (Cu(II)–Cu(II) distances across bridging Cu(I)Br layers) and D_2 (Cu(II)–Cu(II) distance across A^+ cationic layer). (d) Rectangular antiprismatic geometry around A^+ ions coordinated by four formate ions. (e) Striped arrangement of Cu(I) sites in the 2D $[Cu_3Br_4]^{1-}$ layer. (f) Connectivity of [$CuBrO_4$] units and formate ions in the Cu(II)-formate layer within the *ab*-plane, emphasizing interlayer voids filled by A^+ cations. A^+: purple, Cu(I): blue, Cu(II): yellow, C: cyan, O: black, H: grey, Br: red.

Based on bond valence sum calculations, the Cu atoms in the formate layer are in the +2 oxidation state. This single copper(II) site (Cu1, 8*j*) constitutes two Cu(II) ions per formula unit, resulting in an electron-precise semiconducting composition. The copper(II) ions exhibit square pyramidal geometry [CuO_4Br] (Fig. 2b and S9a†), with a base formed by four oxygen atoms from four different bridging formate ions in a μ-$HCOO^{1-}$ anti–anti arrangement and an apical Cu–Br bond. This bridging mode is typical for the formate ion in an environment without bulky ligands.[29,33]

Formate layers are formed *via* corner-sharing, interconnecting linear chains of $Cu_2(COOH)_4$ propagating within the *ab*-plane through Cu(II)–O–C–O–Cu(II) bridges (Fig. 2f). Due to the anti–anti bridging mode of the formate anions (Fig. S9a†), alternating 2D copper formate layers are slightly tilted from one another in the 3D anionic framework. This results in the non-coplanar stacking of alternating copper formate layers (Fig. S9b†). This geometry facilitates the apical Cu(II)–Br bridging, which is crucial in the formation of the 3D anionic framework.

In all the target compounds, the Cu^{2+}–O bond distances vary in the small range of 1.9514(1) to 1.9541(1) Å, and the O–Cu^{2+}–O bond angles are almost 90°. These distances are consistent with those observed for Cu^{2+} oxides and formates.[51,52] The square planar Cu-formate layers are bridged *via* corner-sharing with the $[Cu_3Br_4]^{1-}$ anionic layer through Cu(II)–Br–Cu(I) bonds to form [$Cu^{(2+)}BrO_4$] units with square pyramidal geometry, as shown in Fig. 2b and S9a.† The apical bridging Cu(II)–Br bond distance is 2.7001(2) Å, which is significantly longer than distances for tetrahedral Cu(II) in $CuBr_2$, 2.41 Å, but within the range of distances reported for octahedral Cu(II) in $CsCuBr_3$, 2.46–2.96 Å.[53] In $Cu_3Mg(OH)_6Br_2$ with heteroanionic [Cu(II)O_2Br_4] octahedral fragments, Cu–O distances are 1.972 Å and Cu–Br distances are 2.865 Å.[54]

Cu^{2+} exhibits square pyramidal geometry featuring four short equatorial Cu–O bonds (1.95 Å) and one long apical Cu–Br bond (2.70 Å). This Jahn–Teller elongation is well known among various Cu^{2+}-based compounds.[2,52,55,56] In the absence of the extended apical Cu–Br bonds, the structure would consist of 2D frameworks of Cu-formate and Cu–Br, which are upheld by van der Waals interactions. The elongated apical Cu–Br bond connects these two 2D layers, resulting in the 3D anionic $[Cu_5Br_4(COOH)_4]^-$ framework.

The 3D anionic $[Cu_5Br_4(COOH)_4]^-$ slabs are separated by A^+ cationic layers. A^+ cations adopt a rectangular antiprismatic coordination (Fig. 2d) by oxygen atoms from four formate anions from alternating $Cu_2(COOH)_4$ layers. The resulting $[A(COOH)_4]^{3-}$ units connect to the [$CuBrO_4$] polyhedra, thus linking the anionic slabs together to yield the $ACu_5Br_4(COOH)_4$ structure (Fig. S8†). The A^+ polyhedral volume and $Cu^{2+}\cdots Cu^{2+}$ interatomic distance between alternating slabs are determined by the size of A^+ ions. Attempts to synthesize the Cs and Li analogs were unsuccessful, either due to drastically different synthetic conditions required for Cs and Li, or due to the

 © 2025 The Author(s). Published by the Royal Society of Chemistry

Open Access Article. Published on 05 May 2025. Downloaded on 4/1/2026 6:31:56 PM.
This article is licensed under a Creative Commons Attribution-NonCommercial 3.0 Unported Licence.

destabilization of the 3D framework caused by the extreme ionic radii, Cs^+ being too large and Li^+ too small. Additionally, the failure to synthesize these phases may be attributed to the inability of Cs^+ and Li^+ to adopt the required rectangular antiprismatic coordination, which is essential for the stabilization of the structure. The interlayer $Cu^{2+}\cdots Cu^{2+}$ distances, D_2, for Na^+, K^+, NH_4^+, and Rb^+ analogues are 3.4982(9), 3.8379(3), 4.0871(8), and 4.1547(9) Å, respectively, with A^+ polyhedral volumes ranging between 25.13–34.96 Å^3. The extrapolated $Cu^{2+}\cdots Cu^{2+}$ distances expected for hypothetical Li^+ and Cs^+ analogs are 3.04 and 4.53 Å, respectively. Further details regarding the crystal structure refinement parameters may be obtained from Table S2† and the Cambridge Crystallographic Data Centre by quoting the depository numbers CCDC 2412816–2412819.

Attempts to solve $NaCu_5Br_4(COOH)_4$ within the monoclinic $C2/m$ space group, similar to the other $ACu_5Br_4(COOH)_4$, were unsuccessful. Despite the high quality of synthesized crystals, refinements in $C2/m$ yielded high R_1 values (10.4%) and revealed significant residual electron density around Cu(I) atomic sites in the structure. Based on these observations, we hypothesized that the Na-analogue may exhibit different ordering within the $[Cu_3Br_4]^-$ layers due to the smaller size of Na^+ ions compared to larger A^+ ions. Re-evaluation of the single crystal diffraction data showed the presence of weak superstructural reflections suggesting the $P2_1/c$ space group (no. 14) for $NaCu_5Br_4(COOH)_4$. The structure was successfully solved in $P2_1/c$, resulting in a significantly lower R_1 value of 3.0%. The crystal structure of $NaCu_5Br_4(COOH)_4$ is analogous to the other three compounds based on their structural motifs, connectivity, and bond distances and angles (Tables S3 and S4†), but there are some differences due to the change in symmetry.

In the C-centered structures of the K-, NH_4-, and Rb-analogs, there are one Cu(II) (8*j*) and three Cu(I) (8*j*, 4*h*, and 4*h*) sites. In turn, the asymmetric unit of the primitive $P2_1/c$ structure contains two square pyramidal Cu(II) sites (4*e*) and four tetrahedral Cu(I) sites (4*e*) (Fig. S10 and Table S4†). Notably, the splitting of the 8*j* Cu(I) site in the $C2/m$ model into two 4*e* sites in $P2_1/c$ is accompanied by changes in the site occupancy and ordering of Cu(I) atoms and Cu vacancies within the Cu–Br layer (Fig. S10b†). $NaCu_5Br_4(COOH)_4$ exhibits near-complete ordering of Cu(I) vacancies such that two 4*e* Cu(I) sites are fully occupied while the other two exhibit partial occupancies of approximately 94.1(1)% and 5.9(1)%, respectively. In contrast, other $ACu_5Br_4(COOH)_4$ analogs exhibit 75% occupancy in all Cu(I) sites (Fig. S10a†). Despite the differences in ordering, in both structural models the composition of the Cu–Br layer refines to $[Cu_3Br_4]^{1-}$. Evidently, the Na-analogue closely approximates an idealized arrangement in which three of the 4*e* Cu(I) sites are fully occupied and there are tetrahedral voids in the Cu–Br layer (Fig. S10c†). Contrary, the structures with larger A^+ cations exhibit a random distribution of 25% vacancies among all three Cu(I) crystallographic sites. The $ACu_5Br_4(COOH)_4$ structures are charge balanced, $A^{+1}(Cu^{+2})_2(Cu^{+1})_3(Br^{-1})_4(HCOO^{-1})_4$, thus semiconducting behavior is expected together with potential magnetic and optical properties.

3.3 Thermal properties

The thermal stabilities of the synthesized compounds were studied using a combination of thermogravimetric analysis (TGA) and differential scanning calorimetry (DSC). Three out of the four $ACu_5Br_4(COOH)_4$ compounds ($A^+ = Na^+$, K^+, and Rb^+) showed one TGA weight loss event under an argon atmosphere (Fig. S4a, b and d†). In contrast, their DSC curves reveal multiple thermal events during heating to 400 °C (Fig. S5†). Among these, the prominent endothermic peaks observed above 180 °C can be attributed to the decomposition of residual inorganic $[ACu_5Br_4]$ framework for $A^+ = Na^+$, K^+, and Rb^+. For $A^+ = NH_4^+$ the removal of NH_4/4COOH is completed at 230 °C. This assignment is supported by post-TGA PXRD analysis. The experimental percent weight loss for Na, K, and Rb analogs are close to the expected (calculated) loss of four formate ions per formula unit: 21.6 (21.4), 20.7 (21.0), and 20.5 (19.9), respectively. According to PXRD after these TG-DSC experiments, the loss of formate resulted in the formation of ternary (K_2CuBr_3 and $RbCu_2Br_3$), binary (NaBr and CuBr), and metallic Cu species which remain stable up to 400 °C (Fig. S4–S6†). From DSC, the thermal decomposition steps were mainly exothermic with an estimated energy release between 10–40 kJ mol^{-1}, which is lower than the values observed for other reported metal formate compounds.[33,51]

During the TGA analysis of $NH_4Cu_5Br_4(COOH)_4$, two separate weight losses were observed, accounting for 16.98% and 6.28% of the total weight loss (23.26%), shown in Fig. S4c.† The total weight loss is likely due to removing four formate ions and one ammonium ion (*ca.* 23.7%). However, due to the potential formation of hydrogen bonds between these two species, a more complex mechanism for weight loss might be involved.

3.4 Fourier transform infrared (FTIR) spectroscopy

The FTIR spectra of the measured $ACu_5Br_4(COOH)_4$ (A = NH_4, K, and Rb) compounds are similar, which is expected for isostructural compounds. Characteristic IR bands of $HCOO^-$ were observed (Fig. 3a) and their assignments agree with previous reports for copper formates.[2,33,49] The symmetric ν_s(C=O) and antisymmetric ν_{as}(C=O) stretching vibrations of the $HCOO^-$ ions occur around 1360 cm^{-1} and 1560 cm^{-1}, respectively, revealing the bridging modes of the carboxylate groups.[2] The absence of a split in the O–C–O symmetric deformation band, δ_s(O–C–O) around 800 cm^{-1}, implies all C–O bonds have the same conformation (equatorial). The band centered at ~500 cm^{-1} can be assigned to a Cu–O stretching mode, similar to what has previously been reported.[57,58]

3.5 Linear optical properties

The studied compounds exhibit a dark-yellow color and two distinctive absorption bands in the UV-vis spectra (Fig. 3b). The absorption edge at approximately 30 000 cm^{-1} is attributed to ligand-to-metal charge transfer (LMCT) between Cu^{2+} ions and negatively charged formate ligands.[59–61] Metal-to-ligand charge transfer (MLCT) between Cu^{1+} with a full $3d^{10}$ configuration and Br with a lone pair of electrons in the Cu–Br layers is forbidden

Open Access Article. Published on 05 May 2025. Downloaded on 4/1/2026 6:31:56 PM.
This article is licensed under a Creative Commons Attribution-NonCommercial 3.0 Unported Licence.

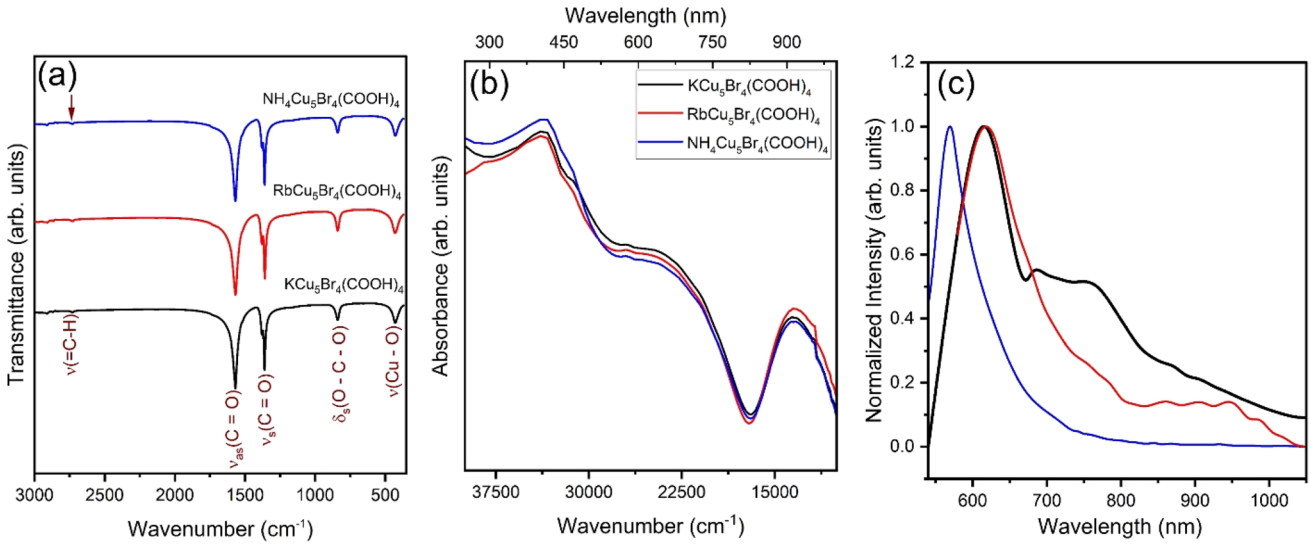

Fig. 3 (a) FTIR spectra showing the various vibration modes, (b) UV-vis absorption, and (c) photoluminescence (PL) spectra collected at 298 K of $ACu_5Br_4(COOH)_4$ compounds, A = K (black), NH_4 (blue), and Rb (red).

because of the π-donating nature of the Br^- ions. However, excitation from the filled 3d orbitals of Cu^{1+} into the empty s/p shells cannot be ruled out given that this absorption band is expected around 32 000 cm^{-1}.[62] Meanwhile, the band centered around 11 000 cm^{-1} is due to the d–d transition of Cu^{2+}, typical of Cu^{2+} species in a non-octahedral local environment.[51,60,62,63] The observed square pyramidal geometry (Fig. 2b) suggests that the d–d band of Cu^{2+} centers occurs due to p–d hybridization. The dark-yellow color of the crystals indicates a band gap of ~2.2 eV, consistent with the observed band edge at 17 500 cm^{-1}. Furthermore, Tauc plots derived from diffuse reflectance spectra reveal direct band gaps between 2.20 and 2.22 eV for NH_4 and Rb analogues, which align well with the estimates from Kubelka–Munk analysis (Fig. S7†). Indirect band gaps were also determined from the Tauc plots, with slightly smaller values (2.13–2.16 eV) than the direct band gaps.

3.6 Photoluminescence properties

Room temperature PL spectroscopy of $ACu_5Br_4(COOH)_4$ reveals a very distinct emission peak (Fig. 3c). The PL emission maxima are at ~600 nm which corresponds to a band-to-band transition of ~2 eV. This is in good agreement with the band gap obtained from diffuse reflectance data and is evident of efficient radiative recombination across the band gap. Additionally, a secondary, broader emission peak is observed for these compounds. The coexistence of mixed-valence Cu^{+1} and Cu^{+2} oxidation states in these compounds suggest the contribution of intervalence charge-transfer (IVCT)[64,65] to the low-energy emission spectra observed in the PL spectra. IVCT transitions typically manifest as broad, lower-energy spectral bands, which could overlap significantly with the d–d transitions of Cu^{2+} (~11 000 cm^{-1}) identified in the UV-vis spectra. In copper complexes with centrosymmetric octahedral environments, the d–d transitions,[62] are generally weak in intensity due to their Laporte-forbidden nature. Such transitions become partially allowed in the non-octahedral non-centrosymmetric Cu local environments. Therefore, the broad and asymmetric nature of the secondary PL peaks likely reflect combined contributions from both IVCT and d–d transitions. Future studies involving temperature-dependent photoluminescence, transient absorption spectroscopy, or electro conductivity measurements will be valuable to clearly distinguish and elucidate the role of IVCT transitions in these compounds. The stability of the PL peaks across multiple measurements underscores the optical robustness of these crystals, suggesting their promise for device applications requiring consistent optical performance.

3.7 Magnetic properties

Exploration of magnetic properties of polycrystalline samples demonstrated a broad hump in the magnetic susceptibility in the 50–300 K range and a sharp transition below 40 K (Fig. 4A). Such a broad hump in susceptibility is typical for low-dimensional 1D or 2D magnetic ordering.[63,66,67] This indicates strong coupling of Cu^{2+} spins in the square formate layer but weak interlayer interactions due to separation by non-magnetic Cu–Br or A^+ layers. Magnetic ordering occurs at slightly different temperatures depending on the nature of the A^+ cation and corresponding Cu^{2+}–Cu^{2+} intra- and interlayer separations (Fig. 4A, S11 and S13†). 3D magnetic ordering observed at low temperatures is of a ferro- or ferrimagnetic nature, which is corroborated by the observation of splitting between FC and ZFC susceptibilities of polycrystalline samples (Fig. S12†). For Rb^+ and NH_4^+, magnetic ordering is a single transition, while for Na^+ and K^+ a two-step transition occurs. At room temperature, the χT values ranged from 0.69–0.98 emu mol^{-1} K^{-1} (Fig. S11†), which is close to the expected value for two isolated Cu^{2+} ions with $S = \frac{1}{2}$ spin states (assuming g-factor = 2) of 0.75 emu mol^{-1} K^{-1}. The effective magnetic moments (μ_{eff}) calculated from these values range from 1.66–1.98μ_B per Cu^{2+}, which differ slightly from the 1.73μ_B expected per Cu^{2+}. However, the

 © 2025 The Author(s). Published by the Royal Society of Chemistry

Open Access Article. Published on 05 May 2025. Downloaded on 4/1/2026 6:31:56 PM.
This article is licensed under a Creative Commons Attribution-NonCommercial 3.0 Unported Licence.

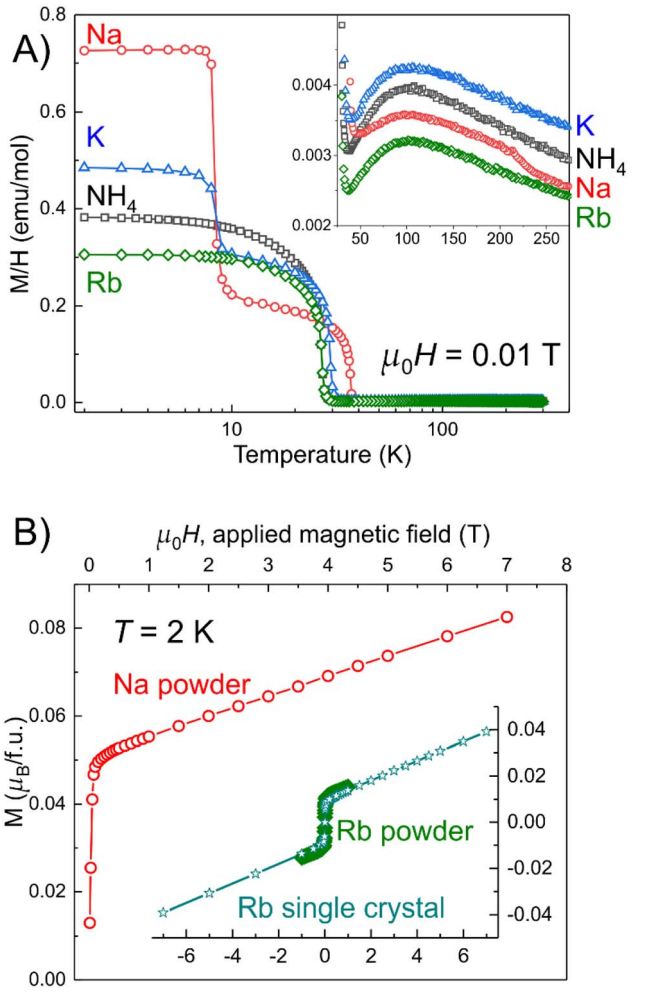

Fig. 4 (A) Temperature dependence of molar susceptibility (M/H) under an applied *dc* magnetic field of 0.01 T for polycrystalline samples of $ACu_5Br_4(COOH)_4$. (Inset) Enlarged region of 45–275 K. (B) Isothermal field dependence at $T = 2$ K of magnetization for a polycrystalline sample of $NaCu_5Br_4(COOH)_4$. (Inset) Comparison of isothermal field dependences of polycrystalline and single crystal samples of $RbCu_5Br_4(COOH)_4$.

experimental $g_{average}$ values (2.17 for $KCu_5Br_4(COOH)_4$) obtained from EPR studies (*vide infra*) result in μ_{eff} of $\sim 1.88\mu_B$ per Cu^{2+}, which is well within the range observed from the χT at room temperature. This consistency between the χT-derived magnetic moments and the EPR-derived g-values confirms that the magnetic nature of the Cu^{2+} ions is intrinsic to the target compounds.

The isothermal magnetization data indicates weakly ferromagnetic or ferrimagnetic behavior characterized by rapid saturation at low applied field followed by a linear increase in magnetization. However, unlike the moments observed from the susceptibility plot, the M *vs.* H plot revealed moments less than $0.1\mu_B$ per Cu^{2+}. To elucidate the source of these disparities, we performed detailed studies of the magnetic properties on selected oriented single crystals (Fig. 4B). For the Rb-containing compound, magnetization appeared to be in line with polycrystalline data (Fig. 4B inset). EPR investigations confirmed that the observed magnetic transitions are intrinsic to the studied compounds (*vide infra*).

To ensure that the observed magnetic properties are intrinsic, we also performed studies on oriented single crystals of $NH_4Cu_5Br_4(COOH)_4$ (Fig. 5). Temperature dependence of magnetic susceptibility for both $H\|c$ and $H\|ab$ orientations at 0.1 T applied magnetic field revealed broad maxima in 50–200 K range, as depicted in the inset of Fig. 5A. This behavior is consistent with that observed in polycrystalline samples. The data, when fitted using a simple Ising model within the 50–200 K temperature range, yielded a coupling constant of $J/k_B = -101$ K, which indicates strong antiferromagnetic (AFM) coupling between Cu^{2+} spins in the square formate layers based on the negative value of J. Details for the fitting and data for other powdered and single crystal samples are provided in the ESI (Fig. S14, 15 and Table S5).† The Ising model is not the most applicable for describing a nearly square 2D lattice of magnetic ions. Due to the absence of an analytical expression for square lattices, polynomial expressions are used for the fitting susceptibility of square-lattice antiferromagnets. However, our

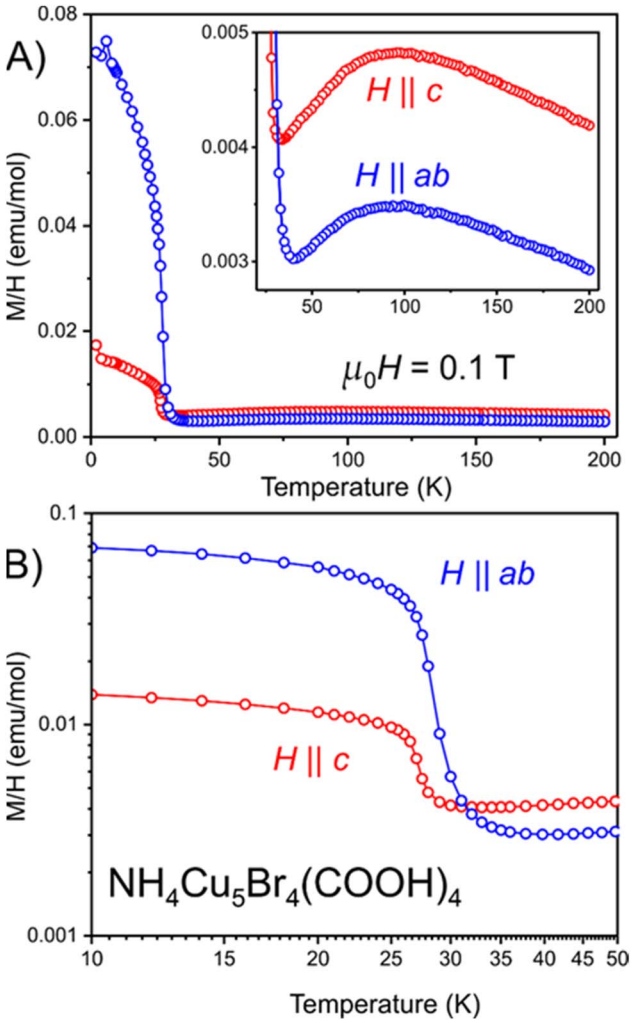

Fig. 5 (A) Temperature dependence of molar susceptibility (M/H) under an applied *dc* magnetic field of 0.1 T for oriented single crystals of $NH_4Cu_5Br_4(COOH)_4$. (Inset) Enlarged region of 50–200 K. (B) Double log plot of the 10–50 K region emphasizing the difference in directional behavior.

Open Access Article. Published on 05 May 2025. Downloaded on 4/1/2026 6:31:56 PM. This article is licensed under a Creative Commons Attribution-NonCommercial 3.0 Unported Licence.

attempts to fit magnetic data to a standard polynomial expression for square-lattice antiferromagnets[39,68] did not yield satisfactory results, probably due to a lack of higher temperature ($T >$ 300 K) data. The weak interlayer magnetic interactions can be attributed to the presence of large, non-magnetic layers such as Cu–Br or A^+ that spatially separate the magnetic layers, reducing the influence of neighboring layers. This suggests that while the in-plane interactions are strong, the system exhibits low-dimensional magnetic behavior with limited interplanar coupling, contributing to the observed magnetic anisotropy.

Higher values of susceptibility were observed with the applied magnetic field oriented along the *c* direction. Assuming the Cu^{2+} magnetic spins are antiferromagnetically coupled in the *ab* plane, applying a magnetic field perpendicular to the plane should result in spin canting and a larger susceptibility for the $H\|c$ curve. Below 35 K, the susceptibility abruptly increases for the $H\|ab$ direction while a smaller increase is observed for the $H\|c$ direction (Fig. 5B). In the 3D ordered state, in-layer remains the easy magnetization direction. The easy magnetization direction along the *ab*-plane in the ordered magnetic state was confirmed for all studied compounds by temperature and field dependent measurements. The abrupt increase in susceptibility indicates the presence of spontaneous magnetization, suggesting long-range ferromagnetic or ferrimagnetic ordering. The observed ferromagnetic-like behavior may arise from spin canting, resulting in weak ferromagnetism. In the AFM Cu-formate layers, the spins of neighboring Cu^{2+} ions may not achieve perfect antiparallel alignment, leading to small uncompensated moments along the canting direction. This spin canting is attributed to weak anisotropic Dzyaloshinskii–Moriya (DM) interactions, which induce a slight tilting of spins and a weak deviation from collinearity – a characteristic feature commonly observed in quasi-2D 3d transition metal antiferromagnets.[44,66,69–77] Further, the possibility of a long-range 3D ferrimagnetic state cannot be entirely ruled out. Neutron diffraction studies are necessary to figure out the exact nature of the ordered state. The observed magnetic moment was quite low, less than $0.1\mu_B$ per Cu^{2+} at 7 T applied magnetic field. Such small moments support weak ferromagnetic or canted antiferromagnetic behavior. We hypothesize that while the 2D intralayer magnetic interactions are relatively strong, there is weak communication between formate layers due to large non-magnetic Cu–Br separating layers. The presence of Cu vacancies in Cu–Br layers may additionally distort the magnetic interactions along the [001] crystallographic direction. To confirm the intrinsic nature of magnetic ordering, we performed EPR investigations.

3.8 Electron paramagnetic resonance (EPR) spectroscopy

EPR spectra of powdered samples of $ACu_5Br_4(COOH)_4$ (A = K, NH_4, Rb) are shown in Fig. 6, S16 and S18.† Above 50 K, a simple spectrum characteristic of monomeric Cu(II) with $g_x = g_y =$ 2.075 and $g_z = 2.350$ is observed for $KCu_5Br_4(COOH)_4$. The observed *g*-values can be attributed to large spin orbit coupling induced by Cu^{2+} ions and agrees with reported values for other Cu(II) complexes with equatorial oxygen coordination.[78,79] The anisotropic nature of the EPR signals indicates the elongated axial coordination environment around the Cu^{2+} centers, as evident from the square pyramidal geometry of Cu^{2+} with an elongated axial Cu(II)–Br bond and four equivalent equatorial Cu(II)–O bonds.

The plot of the resonance field dependence on the microwave frequency is depicted in Fig. 6b. Spectra were measured at different frequencies over the 25 GHz to 495 GHz range (Fig. S19†). Above the transition temperature, there are two resonances with $g_x = g_y = 2.075$ and $g_z = 2.35$ lying on straight lines (solid and dashed blue lines in Fig. 6b) passing through $\nu = 0$, $B = 0$. As temperature decreases below 50 K, this EPR

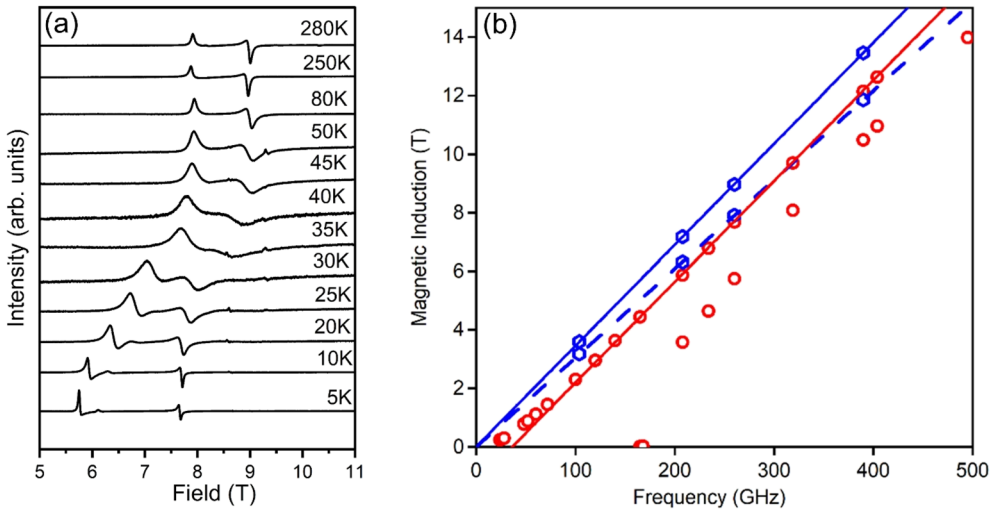

Fig. 6 (a) Temperature-dependent EPR spectra of a powdered sample of $KCu_5Br_4(COOH)_4$ measured at 260 GHz and (b) the resonance field *versus* microwave frequency dependence in $KCu_5Br_4(COOH)_4$, read out from the spectra measured at various microwave frequencies over the range 25 GHz to 495 GHz. The small blue circles represent the resonance fields observed above the transition temperature. The blue solid and dashed lines were calculated using $B = h\nu/(\mu_B \cdot g)$ with $g_x = g_y = 2.075$ and $g_z = 2.350$, respectively. Red open circles represent resonances seen at 3 K. The solid red line was calculated using $B = h\nu/(\mu_B \cdot g) - B_{internal}$, with $g = 2.075$ and $B_{internal}$ equal to 1.25 T.

 © 2025 The Author(s). Published by the Royal Society of Chemistry

Open Access Article. Published on 05 May 2025. Downloaded on 4/1/2026 6:31:56 PM.
This article is licensed under a Creative Commons Attribution-NonCommercial 3.0 Unported Licence.

spectrum is replaced by a very different one, consisting mainly of two strong and sharp resonances which are significantly shifted downfield from their high-temperature positions. The magnitude of the shift increases with decreasing temperature (Fig. 6a, S15a and S17†). This shift is attributed to the development of internal magnetic fields due to 3D ferromagnetic ordering (*vide supra*). The low-temperature resonances lie on a straight line (red in Fig. 6b). The red line is parallel to the solid blue line which represents high-temperature "perpendicular" resonances.

The shift of the red line from the blue line suggests the emergence of the internal magnetic field of ~1.25 T at low temperatures. These values are estimated using the equation $B = h\nu/(\mu_B \cdot g) - B_{\text{internal}}$, using $g_x = g_y = 2.075$. However, none of the low-temperature experimental points align with a line parallel to the dashed blue line which represents the high-temperature "parallel" resonances, indicating that the low-temperature spectra lack the "parallel" spectral features. Similar to $KCu_5Br_4(COOH)_4$, a set of points below the transition temperature are observed in the $NH_4Cu_5Br_4(COOH)_4$ sample with the distinct internal magnetic fields of 1.30 T (Fig. S16b†).

These EPR studies confirm that the observed magnetic features in the studied compounds are intrinsic rather than resulting from admixtures. The detection of low magnetization, less than $0.1\mu_B$ per Cu^{2+} ion, in combination with the high internal magnetic fields (~1.3 T) detected by EPR, points to a complex magnetic ordering along the [001] direction below 40 K. This underscores the intricate magnetic character of the compounds, though the exact origin of this ordering is yet to be determined.

4 Conclusion

We have reported the synthesis of a series of novel hybrid copper formate compounds, showcasing an innovative approach toward a 3D anionic framework by interlinking 2D copper(II) formate and copper(I) bromide layers. Our comprehensive analysis has confirmed the structural integrity and stability of these compounds and illuminated their unique electronic and magnetic characteristics. Notably, strong antiferromagnetic coupling of Cu^{2+} spins in the formate 2D layer was observed while relatively weak interlayer interactions are moderated by large non-magnetic Cu–Br layers. Optical measurements on the dark yellow crystals revealed a bandgap of ~2.2 eV and corroborated d–d and IVCT transitions characteristic of Cu^{2+} in a square pyramidal geometry. This work not only enriches the existing body of knowledge concerning copper formate frameworks but also opens new avenues for the design of materials by stacking layers of various functionality, such as optical and magnetic layers for application in fields including electronics, magnetism, and photonics.

Data availability

The data supporting this article have been included as part of the ESI.† Crystallographic data have been deposited at the Cambridge Crystallographic Data Centre and can be retrieved by quoting the depository numbers CCDC 2412816–2412819.

Author contributions

Yao Abusa, Joshua Greenfield, Gayatri Viswanathan, Smitakshi Goswami, Emma Ross, Philip Yox, Richeal Oppong, Iyanu Ojo, Jifeng Liu, Andrew Ozarowski, Kirill Kovnir: investigation. Kirill Kovnir: supervision. All authors: writing – review & editing.

Conflicts of interest

The authors declare that they have no known competing financial interests or personal relationships that could have appeared to influence the work reported in this paper.

Acknowledgements

This work was supported by the U.S. Department of Energy, Office of Science, Basic Energy Sciences, Division of Materials Science and Engineering, Physical Behavior of Materials program under award number DE-SC0023509. Use of the Advanced Photon Source was supported by U.S. Department of Energy, Office of Basic Energy Sciences, under contract no. DE-AC02-06CH11357. A portion of this work was performed at the National High Magnetic Field Laboratory, which is supported by National Science Foundation Cooperative Agreement no. DMR-2128556 and the State of Florida. The authors would like to thank Colin Unger (UC Davis) for initial work on synthesis of the reported materials; Dr W. Straszheim (MARL-ISU) for the help with SEM/EDS data collection; Prof. J. V. Zaikina (ISU) for access to the UV-vis spectrometer; Dr Brett Boote (CIF-ISU) with help with TG-DSC; Dr S. Lapidus (ANL APS) for help with conducting high-resolution synchrotron PXRD at beamline 11-BM; and Prof. Warren Pickett (UC Davis) for the discussion regarding the electronic structure of the reported materials.

References

1 A. Walsh, Y. Yan, M. N. Huda, M. M. Al-Jassim and S.-H. Wei, Band Edge Electronic Structure of $BiVO_4$: Elucidating the Role of the Bi s and V d Orbitals, *Chem. Mater.*, 2009, **21**(3), 547–551.
2 S.-Y. Zhang, Z.-Z. He, M. Yang, W.-B. Guo and Y.-Y. Tang, Synthesis and Magnetic Properties of a New Polymorph of $Cu_2(VO_4)(OH)$ with a Quasi-2D Layer Structure, *Dalton Trans.*, 2014, **43**(9), 3521–3527.
3 J. Pitcairn, A. Iliceto, L. Cañadillas-Delgado, O. Fabelo, C. Liu, C. Balz, A. Weilhard, S. P. Argent, A. J. Morris and M. J. Cliffe, Low-Dimensional Metal–Organic Magnets as a Route toward the $S = 2$ Haldane Phase, *J. Am. Chem. Soc.*, 2023, **145**(3), 1783–1792.
4 A. E. Thorarinsdottir and T. D. Harris, Metal–Organic Framework Magnets, *Chem. Rev.*, 2020, **120**(16), 8716–8789.
5 J. S. Miller, Magnetically Ordered Molecule-Based Materials, *Chem. Soc. Rev.*, 2011, **40**(6), 3266–3296.

Open Access Article. Published on 05 May 2025. Downloaded on 4/1/2026 6:31:56 PM.
This article is licensed under a Creative Commons Attribution-NonCommercial 3.0 Unported Licence.

6 M. Kurmoo, Magnetic Metal–Organic Frameworks, *Chem. Soc. Rev.*, 2009, **38**(5), 1353–1379.
7 J. T. Greenfield, C. D. Unger, M. Chen, N. Izquierdo, K. E. Woo, V. O. Garlea, S. Kamali and K. Kovnir, A Series of Chiral, Polar, Homospin Topological Ferrimagnets: $M_3(OOCH)_5Cl(OH_2)$ (M = Fe, Co, Ni), *Chem. Mater.*, 2017, **29**(18), 7716–7724.
8 J. T. Greenfield, S. Kamali, N. Izquierdo, M. Chen and K. Kovnir, $NH_4FeCl_2(HCOO)$: Synthesis, Structure, and Magnetism of a Novel Low-Dimensional Magnetic Material, *Inorg. Chem.*, 2014, **53**(6), 3162–3169.
9 S. E. Sebastian, N. Harrison, C. D. Batista, L. Balicas, M. Jaime, P. A. Sharma, N. Kawashima and I. R. Fisher, Dimensional Reduction at a Quantum Critical Point, *Nature*, 2006, **441**(7093), 617–620.
10 K. Kodama, M. Takigawa, M. Horvatić, C. Berthier, H. Kageyama, Y. Ueda, S. Miyahara, F. Becca and F. Mila, Magnetic Superstructure in the Two-Dimensional Quantum Antiferromagnet $SrCu_2(BO_3)_2$, *Science*, 2002, **298**(5592), 395–399.
11 X.-Y. Wang, L. Wang, Z.-M. Wang and S. Gao, Solvent-Tuned Azido-Bridged Co^{2+} Layers: Square, Honeycomb, and Kagomé, *J. Am. Chem. Soc.*, 2006, **128**(3), 674–675.
12 D. Gatteschi and R. Sessoli, Quantum Tunneling of Magnetization and Related Phenomena in Molecular Materials, *Angew. Chem., Int. Ed.*, 2003, **42**(3), 268–297.
13 E. H. Gamage, S. Kamali, J. K. Clark, Y. Lee, P. Yox, P. Shafer, A. A. Yaroslavtsev, L. Ke, M. Shatruk and K. Kovnir, As–Se Pentagonal Linkers to Induce Chirality and Polarity in Mixed-Valent Fe–Se Tetrahedral Chains Resulting in Hidden Magnetic Ordering, *J. Am. Chem. Soc.*, 2022, **144**(25), 11283–11295.
14 E. H. Gamage, J. T. Greenfield, C. Unger, S. Kamali, J. K. Clark, C. P. Harmer, L. Luo, J. Wang, M. Shatruk and K. Kovnir, Tuning Fe–Se Tetrahedral Frameworks by a Combination of $[Fe(en)_3]^{2+}$ Cations and Cl^- Anions, *Inorg. Chem.*, 2020, **59**(18), 13353–13363.
15 E. Coronado, J. R. Galán-Mascarós, C. J. Gómez-García and V. Laukhin, Coexistence of Ferromagnetism and Metallic Conductivity in a Molecule-Based Layered Compound, *Nature*, 2000, **408**(6811), 447–449.
16 H. Tokoro and S. Ohkoshi, Novel Magnetic Functionalities of Prussian Blue Analogs, *Dalton Trans.*, 2011, **40**(26), 6825–6833.
17 M. Anbuchezhiyan, S. Ponnusamy, C. Muthamizhchelvan and K. Sivakumar, Crystal Growth, Structure and Characterizations of a New Semiorganic Nonlinear Optical Material - β-Alanine Zinc Chloride, *Mater. Res. Bull.*, 2010, **45**(8), 897–904.
18 G.-C. Xu, X.-M. Ma, L. Zhang, Z.-M. Wang and S. Gao, Disorder–Order Ferroelectric Transition in the Metal Formate Framework of $[NH_4][Zn(HCOO)_3]$, *J. Am. Chem. Soc.*, 2010, **132**(28), 9588–9590.
19 G.-C. Xu, W. Zhang, X.-M. Ma, Y.-H. Chen, L. Zhang, H.-L. Cai, Z.-M. Wang, R.-G. Xiong and S. Gao, Coexistence of Magnetic and Electric Orderings in the Metal–Formate Frameworks of $[NH_4][M(HCOO)_3]$, *J. Am. Chem. Soc.*, 2011, **133**(38), 14948–14951.
20 M. E. Ziebel, L. E. Darago and J. R. Long, Control of Electronic Structure and Conductivity in Two-Dimensional Metal–Semi quinoid Frameworks of Titanium, Vanadium, and Chromium, *J. Am. Chem. Soc.*, 2018, **140**(8), 3040–3051.
21 K. S. Pedersen, P. Perlepe, M. L. Aubrey, D. N. Woodruff, S. E. Reyes-Lillo, A. Reinholdt, L. Voigt, Z. Li, K. Borup, M. Rouzières, D. Samohvalov, F. Wilhelm, A. Rogalev, J. B. Neaton, J. R. Long and R. Clérac, Formation of the Layered Conductive Magnet $CrCl_2(pyrazine)_2$ through Redox-Active Coordination Chemistry, *Nature Chem*, 2018, **10**(10), 1056–1061.
22 E. H. Gamage, S. Kamali, G. S. Kumar, J. K. Clark, Y. Lee, Y. Abusa, P. Yox, L. Ke, M. Shatruk and K. Kovnir, Inducing Ferrimagnetic Exchange in 1D-FeSe2 Chains Using Heteroleptic Amine Complexes: $[Fe(en)(tren)][FeSe_2]_2$, *Inorg. Chem.*, 2024, **63**(5), 2443–2453.
23 C. P. Landee and M. M. Turnbull, Recent Developments in Low-Dimensional Copper(II) Molecular Magnets, *Eur. J. Inorg. Chem.*, 2013, **2013**(13), 2266–2285.
24 P. Peksa, J. K. Zaręba, M. Ptak, M. Mączka, A. Gągor, S. Pawlus and A. Sieradzki, Revisiting a Perovskite-like Copper-Formate Framework $NH_4[Cu(HCOO)_3]$: Order–Disorder Transition Influenced by Jahn-Teller Distortion and above Room-Temperature Switching of the Nonlinear Optical Response between Two SHG-Active States, *J. Phys. Chem. C*, 2020, **124**(34), 18714–18723.
25 R. Shang, S. Chen, Z.-M. Wang and S. Gao, A Copper–Formate Framework Showing a Simple to Helical Antiferroelectric Transition with Prominent Dielectric Anomalies and Anisotropic Thermal Expansion, and Antiferromagnetism, *Chem.–Eur. J.*, 2014, **20**(48), 15872–15883.
26 V. N. Krasil'nikov, V. P. Zhukov, E. V. Chulkov, I. V. Baklanova, D. G. Kellerman, O. I. Gyrdasova, T. V. Dyachkova and A. P. Tyutyunnik, Novel Method for the Production of Copper(II) Formates, Their Thermal, Spectral and Magnetic Properties, *J. Alloys Compd.*, 2020, **845**, 156208.
27 H. Yoshida, Y. Michiue, E. Takayama-Muromachi and M. Isobe, β-Vesignieite $BaCu_3V_2O_8(OH)_2$: A Structurally Perfect $S = 1/2$ Kagomé Antiferromagnet, *J. Mater. Chem.*, 2012, **22**(36), 18793–18796.
28 M. P. Shores, E. A. Nytko, B. M. Bartlett and D. G. Nocera, A Structurally Perfect $S = 1/2$ Kagomé Antiferromagnet, *J. Am. Chem. Soc.*, 2005, **127**(39), 13462–13463.
29 P. Samarasekere, X. Wang, A. J. Jacobson, J. Tapp and A. Möller, Synthesis, Crystal Structures, Magnetic, and Thermal Properties of Divalent Metal Formate–Formamide Layered Compounds, *Inorg. Chem.*, 2014, **53**(1), 244–256.
30 T.-H. Han, J. S. Helton, S. Chu, D. G. Nocera, J. A. Rodriguez-Rivera, C. Broholm and Y. S. Lee, Fractionalized Excitations in the Spin-Liquid State of a Kagome-Lattice Antiferromagnet, *Nature*, 2012, **492**(7429), 406–410.
31 S. H. Lapidus, J. L. Manson, J. Liu, M. J. Smith, P. Goddard, J. Bendix, C. V. Topping, J. Singleton, C. Dunmars,

 © 2025 The Author(s). Published by the Royal Society of Chemistry

Open Access Article. Published on 05 May 2025. Downloaded on 4/1/2026 6:31:56 PM. This article is licensed under a Creative Commons Attribution-NonCommercial 3.0 Unported Licence.

J. F. Mitchell and J. A. Schlueter, Quantifying Magnetic Exchange in Doubly-Bridged Cu–X_2–Cu (X = F, Cl, Br) Chains Enabled by Solid State Synthesis of CuF_2(Pyrazine), *Chem. Commun.*, 2013, **49**(34), 3558–3560.

32 E. V. Alexandrov, A. V. Virovets, V. A. Blatov and E. V. Peresypkina, Topological Motifs in Cyanometallates: From Building Units to Three-Periodic Frameworks, *Chem. Rev.*, 2015, **115**(22), 12286–12319.

33 Z. Wang, B. Zhang, K. Inoue, H. Fujiwara, T. Otsuka, H. Kobayashi and M. Kurmoo, Occurrence of a Rare 49·66 Structural Topology, Chirality, and Weak Ferromagnetism in the $[NH_4][M^{II}(HCOO)_3]$ (M = Mn, Co, Ni) Frameworks, *Inorg. Chem.*, 2007, **46**(2), 437–445.

34 A. K. Cheetham and C. N. R. Rao, There's Room in the Middle, *Science*, 2007, **318**(5847), 58–59.

35 R. Scatena, R. D. Johnson, P. Manuel and P. Macchi, Formate-Mediated Magnetic Superexchange in the Model Hybrid Perovskite $[(CH_3)_2NH_2]Cu(HCOO)_3$, *J. Mater. Chem. C*, 2020, **8**(37), 12840–12847.

36 C. J. Gómez-García, E. Escrivà, S. Benmansour, J. J. Borràs-Almenar, J.-V. Folgado and C. Ramírez de Arellano, Alternating Ferro/Antiferromagnetic Copper(II) Chain Containing an Unprecedented Triple Formato/Hydroxido/Sulfato Bridge, *Inorg. Chem.*, 2016, **55**(5), 2664–2671.

37 L. Cañadillas-Delgado, L. Mazzuca, O. Fabelo, J. Rodríguez-Carvajal and V. Petricek, Experimental Evidence of the Coexistence of Proper Magnetic and Structural Incommensurability on the $[CH_3NH_3][Ni(COOH)_3]$ Compound, *Inorg. Chem.*, 2020, **59**(24), 17896–17905.

38 J. T. Greenfield, V. Ovidiu Garlea, S. Kamali, M. Chen and K. Kovnir, Synthesis, Crystal Growth, Structural and Magnetic Characterization of NH_4MCl_2(HCOO), M=(Fe, Co, Ni), *J. Solid State Chem.*, 2016, **236**, 222–229.

39 A. Dupas and J.-P. Renard, Zero-Point Spin Deviation and Spontaneous Sublattice Magnetization in the Two-Dimensional Antiferromagnet $Cu(HCOO)_2$. $4D_2O$, *Phys. Lett. A*, 1970, **33**(8), 470–471.

40 B. Dalla Piazza, M. Mourigal, N. B. Christensen, G. J. Nilsen, P. Tregenna-Piggott, T. G. Perring, M. Enderle, D. F. McMorrow, D. A. Ivanov and H. M. Rønnow, Fractional Excitations in the Square-Lattice Quantum Antiferromagnet, *Nat. Phys.*, 2015, **11**(1), 62–68.

41 A. G. Leyva, G. Polla, P. K. de Perazzo, H. Lanza and M. A. R. de Benyacar, Thermal Decomposition of Copper (II) Calcium (II) Formate, *J. Solid State Chem.*, 1996, **123**(2), 291–295.

42 M. J. Sanchis, P. Gomez-Romero, J. V. Folgado, F. Sapina, R. Ibanez, A. Beltran, J. Garcia and D. Beltran, Structural and Magnetic Characterization of Calcium Copper Formates, $CaCu(HCOO)_4$ and $Ca_2Cu(HCOO)_6$: Two New One-Dimensional Ferromagnetic Bis(μ-oxo-Ligand)-Bridged Chains, *Inorg. Chem.*, 1992, **31**(13), 2915–2919.

43 G. Polla, G. Leyva, P. K. de Perazzo, H. Lanza and M. A. R. de Benyacar, Crystal Structure and Thermal Decomposition of Copper(II) Strontium(II) Formate, *J. Solid State Chem.*, 1995, **117**(1), 145–150.

44 L. L. L. Sousa, G. F. Barbosa, F. L. A. Machado, L. R. S. Araujo, P. Brandão, M. S. Reis and D. L. Rocco, Magnetic Dimensionality of Metal Formate $M[(H_2O)_2(HCOO)_2]$ Compounds (M= Co(II), Cu(II)), *IEEE Trans. Magn.*, 2013, **49**(12), 5610–5615.

45 F. Sapina, M. Burgos, E. Escriva, J. V. Folgado, D. Marcos, A. Beltran and D. Beltran, Ferromagnetism and the .Alpha. and .Beta. Polymorphs of Anhydrous Copper(II) Formate: Two Molecular-Based Ferromagnets with Ordering Temperatures of 8.2 and 30.4 K, *Inorg. Chem.*, 1993, **32**(20), 4337–4344.

46 M. Viertelhaus, H. Henke, C. E. Anson and A. K. Powell, Solvothermal Synthesis and Structure of Anhydrous Manganese(II) Formate, and Its Topotactic Dehydration from Manganese(II) Formate Dihydrate, *Eur. J. Inorg. Chem.*, 2003, **2003**(12), 2283–2289.

47 R. D. Pierce and S. A. Friedberg, Heat Capacity of $Mn(HCOO)_2.2H_2O$ between 1.4 and 20 K, *Phys. Rev.*, 1968, **165**(2), 680–687.

48 R. D. Pierce and S. A. Friedberg, Heat Capacities of $Fe(HCOO)_2.2H_2O$ and $Ni(HCOO)_2.2H_2O$ between 1.4 and 20 K, *Phys. Rev. B*, 1971, **3**(3), 934–942.

49 Z. Wang, B. Zhang, T. Otsuka, K. Inoue, H. Kobayashi and M. Kurmoo, Anionic NaCl-Type Frameworks of $[Mn^{II}(HCOO)_3^-]$, Templated by Alkylammonium, Exhibit Weak Ferromagnetism, *Dalton Trans.*, 2004, (15), 2209–2216.

50 H. Kageyama, D. I. Khomskii, R. Z. Levitin and A. N. Vasil'ev, Weak Ferrimagnetism, Compensation Point, and Magnetization Reversal in $Ni(HCOO)_2.2H_2O$, *Phys. Rev. B:Condens. Matter Mater. Phys.*, 2003, **67**(22), 224422.

51 K.-L. Hu, M. Kurmoo, Z. Wang and S. Gao, Metal–Organic Perovskites: Synthesis, Structures, and Magnetic Properties of $[C(NH_2)_3][M^{II}(HCOO)_3]$ (M=Mn, Fe, Co, Ni, Cu, and Zn; $C(NH_2)_3$= Guanidinium), *Chem.–Eur. J.*, 2009, **15**(44), 12050–12064.

52 Y.-M. Li, C.-Y. Xiao, X.-D. Zhang, Y.-Q. Xu, H.-J. Lun and J.-Y. MnI. I. Niu, Cu^{II} and Co^{II} Coordination Polymers Showing Antiferromagnetism, and the Coexistence of Spin Frustration and Long Range Magnetic Ordering, *CrystEngComm*, 2013, **15**(38), 7756–7762.

53 O. Oeckler and A. Simon, Redetermination of the crystal structure of copper dibromide, $CuBr_2$, *Z. fur Krist.–New Cryst. Struct.*, 2000, **215**(1), 13.

54 Y. Wei, Z. Feng, C. dela Cruz, W. Yi, Z. Y. Meng, J.-W. Mei, Y. Shi and S. Li, Antiferromagnetism in the Kagome-Lattice Compound α-$Cu_3Mg(OH)_6Br_2$, *Phys. Rev. B*, 2019, **100**(15), 155129.

55 G. Ji and Z. Xiao, Jahn−Teller Distortion-Stabilized Halide Double Perovskites with Unusual Rock-Salt-Type Ordering of Divalent B-Site Cations, *Chem. Mater.*, 2022, **34**(18), 8207–8212.

56 A. Pasquarello, I. Petri, P. S. Salmon, O. Parisel, R. Car, É. Tóth, D. H. Powell, H. E. Fischer, L. Helm and A. E. Merbach, First Solvation Shell of the Cu(II) Aqua Ion: Evidence for Fivefold Coordination, *Science*, 2001, **291**(5505), 856–859.

Open Access Article. Published on 05 May 2025. Downloaded on 4/1/2026 6:31:56 PM. This article is licensed under a Creative Commons Attribution-NonCommercial 3.0 Unported Licence.

57 Z. Dong, Z. Mi, W. Shi, H. Jiang, Y. Zheng and K. Yang, High Pressure Effects on Hydrate Cu-BTC Investigated by Vibrational Spectroscopy and Synchrotron X-Ray Diffraction, *RSC Adv.*, 2017, 7(87), 55504–55512.

58 J. Ethiraj, F. Bonino, C. Lamberti and S. Bordiga, H_2S Interaction with HKUST-1 and ZIF-8 MOFs: A Multitechnique Study, *Microporous Mesoporous Mater.*, 2015, **207**, 90–94.

59 E. Borfecchia, S. Maurelli, D. Gianolio, E. Groppo, M. Chiesa, F. Bonino and C. Lamberti, Insights into Adsorption of NH3 on HKUST-1 Metal–Organic Framework: A Multitechnique Approach, *J. Phys. Chem. C*, 2012, **116**(37), 19839–19850.

60 C. Prestipino, L. Regli, J. G. Vitillo, F. Bonino, A. Damin, C. Lamberti, A. Zecchina, P. L. Solari, K. O. Kongshaug and S. Bordiga, Local Structure of Framework Cu(II) in HKUST-1 Metallorganic Framework: Spectroscopic Characterization upon Activation and Interaction with Adsorbates, *Chem. Mater.*, 2006, **18**(5), 1337–1346.

61 Z. Guo, J. Li, C. Wang, R. Liu, J. Liang, Y. Gao, J. Cheng, W. Zhang, X. Zhu, R. Pan and T. He, Giant Optical Activity and Second Harmonic Generation in 2D Hybrid Copper Halides, *Angew. Chem., Int. Ed.*, 2021, **60**(15), 8441–8445.

62 T. F. Pascher, M. Ončák, C. van der Linde and M. K. Beyer, UV/Vis Spectroscopy of Copper Formate Clusters: Insight into Metal-Ligand Photochemistry, *Chem.–Eur. J.*, 2020, **26**(37), 8286–8295.

63 H. Zheng, R. Zhang, X. Wu, Q. Zhang, Z. Wu, W. P. D. Wong, J. Chen, Q.-H. Xu and K. P. Loh, Strain-Driven Solid–Solid Crystal Conversion in Chiral Hybrid Pseudo-Perovskites with Paramagnetic-to-Ferromagnetic Transition, *J. Am. Chem. Soc.*, 2023, **145**(6), 3569–3576.

64 B. A. Connor, R. W. Smaha, J. Li, A. Gold-Parker, A. J. Heyer, M. F. Toney, Y. S. Lee and H. I. Karunadasa, Alloying a Single and a Double Perovskite: A $Cu^{+/2+}$ Mixed-Valence Layered Halide Perovskite with Strong Optical Absorption, *Chem. Sci.*, 2021, **12**(25), 8689–8697.

65 J. Li, R. Matheu, F. Ke, Z. Liu, Y. Lin and H. I. Karunadasa, Mosaic Cu^{I}–Cu^{II}–In^{III} 2D Perovskites: Pressure-Dependence of the Intervalence Charge Transfer and a Mechanochemical Alloying Method, *Angew. Chem., Int. Ed.*, 2023, **62**(20), e202300957.

66 S.-H. Park, I.-H. Oh, S. Park, Y. Park, J. H. Kim and Y.-D. Huh, Canted Antiferromagnetism and Spin Reorientation Transition in Layered Inorganic–Organic Perovskite $(C_6H_5CH_2CH_2NH_3)_2MnCl_4$, *Dalton Trans.*, 2012, **41**(4), 1237–1242.

67 L. Septiany, D. Tulip, M. Chislov, J. Baas and G. R. Blake, Polar Structure and Two-Dimensional Heisenberg Antiferromagnetic Properties of Arylamine-Based Manganese Chloride Layered Organic–Inorganic Perovskites, *Inorg. Chem.*, 2021, **60**(20), 15151–15158.

68 J. Darriet, M. S. Haddad, E. N. Duesler and D. N. Hendrickson, Crystal Structure and Magnetic Properties of Bis(Pyrazine)Copper(II) Perchlorate, $Cu(Pyz)_2(ClO_4)_2$, a Two-Dimensional Heisenberg Antiferromagnet, *Inorg. Chem.*, 1979, **18**(10), 2679–2682.

69 D. Coffey, K. S. Bedell and S. A. Trugman, Effective Spin Hamiltonian for the CuO Planes in La_2CuO_4 and Metamagnetism, *Phys. Rev. B:Condens. Matter Mater. Phys.*, 1990, **42**(10), 6509–6514.

70 W. D. van Amstel and L. J. de Jongh, Magnetic Measurements on $(CH_3NH_3)_2MnCl_4$, a Quasi Two-Dimensional Heisenberg Antiferromagnet, *Solid State Commun.*, 1972, **11**(10), 1423–1429.

71 K. W. Lee, C. H. Lee, C. E. Lee and J. K. Kang, Magnetic Ordering in Two-Dimensional Heisenberg Antiferromagnets with Variable Interlayer Distances, *Phys. Rev. B*, 2000, **62**(1), 95–98.

72 D. B. Losee, K. T. McGregor, W. E. Estes and W. E. Hatfield, 1,3-Propanediammonium Tetrachloromanganate(II) $(NH_3CH_2CH_2CH_2NH_3)MnCl_4$: A Canted Quasi-Two-Dimensional Antiferromagnet, *Phys. Rev. B*, 1976, **14**(9), 4100–4105.

73 H. A. Groenendijk, A. J. van Duyneveldt and R. D. Willett, Spin Canting and Exchange in the Two-Dimensional Antiferromagnets $(C_3H_7NH_3)_2$ and $(C_3H_7NH_3)_2MnBr_4$, *Physica B+C*, 1979, **98**(1), 53–59.

74 S.-H. Park, M.-H. Jung, Y.-J. Lee and Y.-D. Huh, Confined Condensation Synthesis and Magnetic Properties of Layered Copper Hydroxide Frameworks, *Dalton Trans.*, 2017, **46**(10), 3363–3368.

75 M. Kubus, A. Lanza, R. Scatena, L. H. R. Dos Santos, B. Wehinger, N. Casati, C. Fiolka, L. Keller, P. Macchi, C. Rüegg and K. W. Krämer, Quasi-2D Heisenberg Antiferromagnets $[CuX(pyz)_2](BF_4)$ with X = Cl and Br, *Inorg. Chem.*, 2018, **57**(9), 4934–4943.

76 F. M. Woodward, P. J. Gibson, G. B. Jameson, C. P. Landee, M. M. Turnbull and R. D. Willett, Two-Dimensional Heisenberg Antiferromagnets: Syntheses, X-Ray Structures, and Magnetic Behavior of $[Cu(pz)_2](ClO_4)_2$, $[Cu(pz)_2](BF_4)_2$, and $[Cu(pz)_2(NO_3)](PF_6)$, *Inorg. Chem.*, 2007, **46**(10), 4256–4266.

77 T. Matsumoto, Y. Miyazaki, A. S. Albrecht, C. P. Landee, M. M. Turnbull and M. Sorai, Heat Capacities of the $S = 1/2$ Two-Dimensional Heisenberg Antiferromagnet Bis(2-Amino-5-Chloropyridinium) Tetrabromocuprate(II) $[(5CAP)_2CuBr_4]$ and Its Diamagnetic Analogue $[(5CAP)_2ZnBr_4]$, *J. Phys. Chem. B*, 2000, **104**(43), 9993–10000.

78 H. M. Zhang, W. B. Xiao and X. Wan, Theoretical Studies of the EPR Parameters and Local Structures for the Two Cu^{2+} Centers in $Cd(HCOO)_2 \cdot 2H_2O$, *Magn. Reson. Chem.*, 2018, **56**(5), 305–310.

79 S. Kiczka, S. K. Hoffmann, J. Goslar and L. Szczepanska, Electronic Structure, Jahn–Teller Dynamics and Electron Spin Relaxation of Two Types of Octahedral Cu(II) Complexes in Cadmium Formate Dihydrate $Cd(HCOO)_2 \cdot 2H_2O$. EPR and ESE Studies, *Phys. Chem. Chem. Phys.*, 2004, **6**(1), 64–71.

 © 2025 The Author(s). Published by the Royal Society of Chemistry